Research Square

Preprints are preliminary reports that have not undergone peer review.
They should not be considered conclusive, used to inform clinical practice,
or referenced by the media as validated information.

Multimodal MR Radiomics for Preoperative Prediction of Perineural Invasion and Prognostic Stratification in Intrahepatic Cholangiocarcinoma

Da He
Eastern Hepatobiliary Surgery Hospital Naval Medical University
Sisi Zhang
Eastern Hepatobiliary Surgery Hospital Naval Medical University
Dong Liu
Eastern Hepatobiliary Surgery Hospital Naval Medical University
Helin Li
Eastern Hepatobiliary Surgery Hospital Naval Medical University
Changzhou Shi
Eastern Hepatobiliary Surgery Hospital Naval Medical University
Hao Shen
Eastern Hepatobiliary Surgery Hospital Naval Medical University
Ningyang Jia
ningyangjia@163.com
Eastern Hepatobiliary Surgery Hospital Naval Medical University
Feng Shen
Eastern Hepatobiliary Surgery Hospital Naval Medical University

Research Article

Keywords: intrahepatic cholangiocarcinoma, perineural invasion, radiomics, multimodal model, magnetic resonance imaging, survival

Posted Date: November 5th, 2026

DOI: https://doi.org/10.21203/rs.3.rs-11345737/v1

License: This work is licensed under a Creative Commons Attribution 4.0 International License.
Read Full License

Additional Declarations: No competing interests reported.

Abstract

Background

To develop and validate a multimodal model integrating multiphasic contrast-enhanced MRI radiomics with clinical-imaging information for the preoperative prediction of perineural invasion (PNI) in intrahepatic cholangiocarcinoma (ICC) and for postoperative risk stratification.

Methods

Patients with ICC treated at the Eastern Hepatobiliary Surgery Hospital between September 2014 and February 2025 were retrospectively enrolled (*n* = 455) and randomly assigned to training (*n* = 232), testing (*n* = 99) and validation (*n* = 124) cohorts. Radiomic features were extracted with PyRadiomics from tumor regions on all four phases and selected by LASSO regression; the clinical-imaging, radiomics and multimodal models were built with logistic regression. Discrimination, calibration and clinical net benefit were assessed by the area under the receiver operating characteristic curve (AUC), calibration curves and decision curve analysis (DCA). Overall survival (OS) and recurrence-free survival (RFS) were compared by the Kaplan-Meier

1. Introduction

Intrahepatic cholangiocarcinoma (ICC) originates from the intrahepatic biliary epithelium, accounts for approximately 10%–20% of primary liver malignancies, and shows a continually rising incidence worldwide [1–3]. Radical resection is the only potentially curative treatment, but postoperative recurrence is frequent and long-term survival remains unsatisfactory [2, 3]. Perineural invasion (PNI), defined as tumor invasion of the perineurium, endoneurium or perineural space, is a route of spread independent of lymphatic and vascular invasion [4, 5], and is an independent adverse prognostic factor for overall survival (OS) and recurrence-free survival (RFS) after curative resection of ICC, associated with positive margins, local recurrence and resistance to adjuvant therapy [6–10]; it has therefore been incorporated into postoperative risk stratification [6, 7].

Because PNI is a microscopic finding that can only be confirmed in the surgical specimen, it cannot be assessed before surgery. Conventional CT and MRI depict only indirect signs and have limited sensitivity and specificity for microscopic nerve involvement, and their interpretation is highly subjective [4, 5, 11]. Surgical planning, neoadjuvant decisions and prognostic assessment are therefore made without an objective basis, making a non-invasive preoperative predictor of PNI an unmet clinical need.

Radiomics enables the high-throughput extraction of quantitative features from medical images and captures tumor heterogeneity that is invisible to the naked eye, providing a feasible means of preoperative PNI prediction [11–16]. Models based on contrast-enhanced CT or MRI have shown favorable performance [12, 14, 17], and systematic reviews support the preoperative prediction of ICC

pathology by radiomics [11, 14]; peritumoral features, multiphasic information and multimodal integration with clinical data are regarded as the main directions for improvement [12, 18, 19].

However, most previous studies used a single phase or merged all phases into one high-dimensional feature space, a strategy that is prone to collinearity, and the prognostic value of such models is rarely reported. In the present study, features were therefore selected separately for each phase of multiphasic contrast-enhanced MRI (T2WI, AP, PVP and DP) in 455 patients with ICC, and a clinical-imaging model, a radiomics model and a multimodal model were compared in terms of discrimination, calibration and clinical net benefit; the value of radiomics-based risk stratification for postoperative OS and RFS was also assessed.

2. Materials and methods

2.1 Study population

Patients with ICC confirmed by surgical pathology who were treated at two campuses of the Eastern Hepatobiliary Surgery Hospital between September 2014 and February 2025 were retrospectively enrolled (*n* = 1049). Patients with incomplete preoperative clinical data or images (*n* = 178), without follow-up records extending more than one month after surgery (*n* = 395) or receiving any clinical treatment before MRI (*n* = 21) were excluded, leaving 455 patients for analysis (Fig. 1). The 455 patients were randomly divided into training (232), testing (99) and validation (124) cohorts. The overall workflow is shown in Fig. 2.

2.2 MRI examination

All patients underwent liver MRI within 2 weeks before surgery on a 3.0-T MR scanner (Discovery MR750, GE Healthcare, Milwaukee, WI, USA). The imaging protocol comprised T2-weighted imaging (T2WI) and dynamic contrast-enhanced scanning (arterial phase, AP; portal venous phase, PVP; delayed phase, DP); all four phases were used for radiomics analysis. No patient had received locoregional or systemic antitumor therapy before MRI.

2.3 Image segmentation and feature extraction

Tumor regions of interest (ROIs) were delineated manually, slice by slice, on T2WI, AP, PVP and DP images in ITK-SNAP by two radiologists with more than 5 years of experience in abdominal imaging. The ROIs encompassed the entire tumor parenchyma while avoiding adjacent vessels, bile ducts and normal liver tissue, and the radiologists were blinded to pathological results. The ROIs of 30 randomly selected patients were delineated independently by both radiologists to assess inter-observer agreement, which was quantified with the intraclass correlation coefficient; discrepancies were resolved by consensus. Delineation was performed on every slice containing tumor. Delineation of the portal venous phase is illustrated in Fig. 3 and that of the other phases in Supplementary Figure S1.

Preprocessing, including voxel resampling and gray-level discretization, and feature extraction were performed with PyRadiomics in Python. For each patient and each phase, 1197 radiomic features were extracted, comprising first-order statistics, shape features (original images only), texture features (GLCM, GLDM, GLRLM, GLSZM and NGTDM), and features derived after Laplacian of Gaussian (LoG; σ = 2, 3, 4 and 5 mm) filtering and wavelet transformation (HHH, LLL, HLH, LHH, HLL, LLH, HHL and LHL).

2.4 Feature selection and model construction

Feature selection was performed separately for each phase and the selected features were then combined. For each phase, the following steps were performed: (1) features with $P < 0.05$ in the Mann-Whitney U test between PNI-positive and PNI-negative patients were retained; (2) redundancy was removed by hierarchical clustering of features with $|r| \geq 0.9$ on Spearman correlation, retaining the feature with the smallest P value in each cluster; and (3) L1-penalized logistic LASSO regression with 10-fold cross-validation repeated 5 times was applied, and the 1-SE rule was used to define the final features [20]. Cross-validation was used to limit the risk of overfitting. Five, four, eight and four features were selected for the four phases, giving 21 features in total.

Three models were built: (1) the radiomics model, a logistic regression model based on the 21 features; (2) the clinical-imaging model, a multivariable logistic regression model with backward elimination using clinical, laboratory and MRI variables with $P < 0.05$ in univariable analysis as candidates, which retained Log10 CA19-9 and the biliary dilatation sign; and (3) the multimodal model, a logistic regression model using the predicted probabilities of the clinical-imaging and radiomics models as inputs.

2.5 Model evaluation

The area under the receiver operating characteristic curve (AUC) was the primary measure of discrimination, and 95% confidence intervals (CIs) were calculated with the DeLong method [21]. The classification threshold of each model was set at the point of the maximum Youden index in the training cohort and was kept fixed in the testing and validation cohorts, and sensitivity (SEN), specificity (SPE), accuracy (ACC), positive predictive value (PPV) and negative predictive value (NPV) were derived accordingly. DeLong tests were used to compare different models within a cohort (paired) and the same model between cohorts (unpaired). Calibration was assessed by calibration curves, the Hosmer-Lemeshow test (10 risk groups) and the Brier score, and clinical utility by decision curve analysis (DCA) using net benefit relative to the treat-all and treat-none lines [22]. Calibration curves were smoothed using locally weighted regression (LOESS).

2.6 Survival analysis

Patients were grouped according to PNI status and according to the median predicted probability of the multimodal model (low-risk vs high-risk). OS and RFS were analyzed by the Kaplan-Meier method and the log-rank test, and unadjusted hazard ratios (HRs) with 95% CIs were estimated by univariable Cox regression. The one-, three- and five-year OS and RFS rates and the median follow-up were calculated.

2.7 Statistical analysis

Normally distributed continuous variables are expressed as mean ± standard deviation and compared by the t test or analysis of variance; skewed variables are expressed as median (interquartile range) and compared by the Mann-Whitney U or Kruskal-Wallis test. Categorical variables are expressed as frequencies (percentages) and compared by the chi-square test. Two-sided $P < 0.05$ was considered significant. Analyses were performed with Python 3.12.14 and SPSS Statistics 27. Normality was assessed with the Shapiro-Wilk test.

3. Results

3.1 Baseline characteristics

PNI was present in 92 of the 455 patients (20.2%); the proportions were 42/232 (18.1%), 20/99 (20.2%) and 30/124 (24.2%) in the training, testing and validation cohorts, respectively ($P = 0.395$). Compared with PNI-negative patients, PNI-positive patients had higher CEA ($P = 0.005$), CA19-9 ($P < 0.001$) and GGT ($P = 0.020$) levels, more irregular tumor morphology ($P = 0.007$) and a higher grade of the biliary dilatation sign ($P < 0.001$), but less hepatic capsular retraction ($P = 0.015$); the remaining variables did not differ (Supplementary Table S1). Age, sex, hepatitis B status and maximum tumor diameter were also comparable between the two groups. Baseline data of the three cohorts are given in Table 1.

Table 1
Baseline characteristics of the 455 patients according to dataset (training, testing and validation cohorts).

Variable	Overall (*n* = 455)	Training (*n* = 232)	Testing (*n* = 99)	Validation (*n* = 124)	*P* value
No. of patients	455	232	99	124	
PNI positive	92 (20.2)	42 (18.1)	20 (20.2)	30 (24.2)	0.395
Clinical and demographic					
Age, years	59 (52–67)	61 (52–67)	57 (52–64)	59 (52–67)	0.431
Sex					0.185
Female	165 (36.3)	92 (39.7)	36 (36.4)	37 (29.8)	
Male	290 (63.7)	140 (60.3)	63 (63.6)	87 (70.2)	
Hepatitis B virus infection					0.788
Negative	270 (60.7)	136 (59.6)	63 (63.6)	71 (60.2)	
Positive	175 (39.3)	92 (40.4)	36 (36.4)	47 (39.8)	
Laboratory findings					
AFP, ng/mL	3.1 (2.0–5.7)	3.2 (2.1–5.1)	2.8 (2.0–5.9)	3.1 (2.0–5.9)	0.812
CEA, ng/mL	2.6 (1.6–4.2)	2.5 (1.6–4.2)	2.5 (1.5–3.8)	2.7 (1.6–4.2)	0.584
CA19-9, U/mL	36.2 (13.3–199)	38.6 (14.2–185)	28.2 (9.8–126)	45.0 (14.5–304)	0.087
Total bilirubin, μmol/L	12.2 (9.8–15.6)	12.1 (9.7–15.4)	12.2 (9.6–15.4)	12.4 (9.9–16.5)	0.567
Direct bilirubin, μmol/L	4.2 (3.2–5.6)	4.1 (3.2–5.5)	4.2 (3.3–5.5)	4.2 (3.2–5.6)	0.900
Total protein, g/L	68.8 ± 5.7	68.9 ± 5.5	69.1 ± 6.0	68.2 ± 5.8	0.436
Albumin, g/L	42.1 (40.0–44.5)	42.2 (40.0–44.2)	42.1 (40.1–45.2)	42.0 (40.1–44.5)	0.692
Cholinesterase, U/L	7026 (6056–8150)	6876 (6158–7984)	7350 (5851–8884)	6932 (5815–8359)	0.289
ALT, U/L	21 (14–31)	21 (15–31)	22 (14–33)	20 (14–32)	0.851
AST, U/L	23 (18–31)	23 (18–30)	23 (18–30)	23 (18–31)	0.905

Variable	Overall (*n* = 455)	Training (*n* = 232)	Testing (*n* = 99)	Validation (*n* = 124)	*P* value
GGT, U/L	54 (29–106)	58 (27–108)	44 (28–120)	56 (32–98)	0.656
PIVKA-II, mAU/mL	23 (19–30)	23 (18–29)	23 (19–33)	24 (20–29)	0.210
MRI findings					
Tumor morphology					0.048
Spherical or ovoid	299 (65.7)	154 (66.4)	60 (60.6)	85 (68.5)	
Lobulated	115 (25.3)	61 (26.3)	32 (32.3)	22 (17.7)	
Irregular	41 (9.0)	17 (7.3)	7 (7.1)	17 (13.7)	
Tumor number					0.279
Single	390 (85.7)	203 (87.5)	86 (86.9)	101 (81.5)	
Multiple	65 (14.3)	29 (12.5)	13 (13.1)	23 (18.5)	
Maximum tumor diameter, cm	4.8 (3.3–7.1)	4.7 (3.4–7.2)	4.8 (3.3–6.5)	5.1 (3.5–7.5)	0.297
T2-weighted signal intensity					< 0.001
Hypointense	3 (0.7)	1 (0.4)	2 (2.0)	0 (0.0)	
Isointense	41 (9.0)	29 (12.5)	12 (12.1)	0 (0.0)	
Hyperintense	411 (90.3)	202 (87.1)	85 (85.9)	124 (100.0)	
Targetoid sign on T1WI-FS					< 0.001
Absent	395 (86.8)	190 (81.9)	82 (82.8)	123 (99.2)	
Present	60 (13.2)	42 (18.1)	17 (17.2)	1 (0.8)	
DWI signal intensity					0.121
Hypointense	3 (0.7)	3 (1.3)	0 (0.0)	0 (0.0)	
Isointense	10 (2.2)	7 (3.0)	3 (3.0)	0 (0.0)	
Hyperintense	441 (97.1)	221 (95.7)	96 (97.0)	124 (100.0)	
Targetoid sign on DWI					0.022
Absent	286 (62.9)	134 (57.8)	62 (62.6)	90 (72.6)	
Present	169 (37.1)	98 (42.2)	37 (37.4)	34 (27.4)	

Variable	Overall (*n* = 455)	Training (*n* = 232)	Testing (*n* = 99)	Validation (*n* = 124)	*P* value
Arterial phase hyperenhancement					0.341
Non-ring	266 (58.5)	133 (57.3)	54 (54.5)	79 (63.7)	
Ring-like	189 (41.5)	99 (42.7)	45 (45.5)	45 (36.3)	
Dynamic enhancement pattern					0.571
Type 1	134 (29.5)	72 (31.0)	26 (26.3)	36 (29.0)	
Type 2	234 (51.4)	113 (48.7)	58 (58.6)	63 (50.8)	
Type 3	87 (19.1)	47 (20.3)	15 (15.2)	25 (20.2)	
Hepatic capsular retraction					0.614
Absent	347 (76.3)	181 (78.0)	75 (75.8)	91 (73.4)	
Present	108 (23.7)	51 (22.0)	24 (24.2)	33 (26.6)	
Biliary dilatation sign					0.496
Grade 0	366 (80.4)	180 (77.6)	84 (84.8)	102 (82.3)	
Grade 1	27 (5.9)	19 (8.2)	4 (4.0)	4 (3.2)	
Grade 2	50 (11.0)	26 (11.2)	9 (9.1)	15 (12.1)	
Grade 3	12 (2.6)	7 (3.0)	2 (2.0)	3 (2.4)	
Visible vessel penetration					0.182
Absent	350 (76.9)	174 (75.0)	83 (83.8)	93 (75.0)	
Present	105 (23.1)	58 (25.0)	16 (16.2)	31 (25.0)	
Adjacent organ invasion					0.002
Absent	297 (65.3)	152 (65.5)	77 (77.8)	68 (54.8)	
Present	158 (34.7)	80 (34.5)	22 (22.2)	56 (45.2)	
Peritumoral enhancement					0.763
Absent	240 (52.9)	121 (52.2)	55 (56.1)	64 (51.6)	
Present	214 (47.1)	111 (47.8)	43 (43.9)	60 (48.4)	

Values are numbers (percentages) unless otherwise indicated. Continuous variables are presented as median (interquartile range) and were compared with the Mann-Whitney U test; categorical variables were compared with the chi-square test. PNI, perineural invasion.

3.2 Radiomic feature selection

A total of 1197 radiomic features were extracted per phase. After the Mann-Whitney U test ($P < 0.05$), 663, 37, 92 and 194 features remained for T2WI, AP, PVP and DP; after Spearman clustering ($|r| \geq 0.9$), 91, 17, 25 and 41 remained; and after LASSO regression with the 1-SE rule, 5, 4, 8 and 4 features were selected, giving 21 features in total (Supplementary Table S2 and Fig. 4). The selected features comprised 15 first-order statistics, 3 GLSZM, 2 GLCM and 1 shape feature, and included 5 wavelet-HLL, 5 LoG σ = 5.0 mm and 4 LoG σ = 2.0 mm features. The remaining features were wavelet-LHL, HHL, HHH, LLL and original-image features.

3.3 Clinical and imaging findings

In univariable logistic regression, Log10 CA19-9 (OR = 2.71, 95% CI 1.69–4.34; $P < 0.001$), Log10 CEA (OR = 2.70, 95% CI 1.49–4.88; $P = 0.001$), tumor morphology (OR = 1.92, 95% CI 1.18–3.13; $P = 0.009$) and the biliary dilatation sign (OR = 2.09, 95% CI 1.46–2.99; $P < 0.001$) were associated with a higher risk of PNI, whereas hepatic capsular retraction was associated with a lower risk (OR = 0.32, 95% CI 0.11–0.94; $P = 0.039$) (Table 2). In the multivariable model, Log10 CA19-9 (OR = 2.30, 95% CI 1.41–3.77; $P < 0.001$) and the biliary dilatation sign (OR = 1.78, 95% CI 1.22–2.60; $P = 0.003$) remained independently associated with PNI (Table 2). The remaining clinical, laboratory and imaging variables were not significantly associated with PNI in either analysis.

Table 2
Univariable and multivariable logistic regression for perineural invasion in the training cohort.

Variable	Univariable OR (95% CI)	*P* value	Multivariable OR (95% CI)	*P* value
Laboratory findings				
Log10 CEA (per unit)	2.70 (1.49–4.88)	0.001		
Log10 CA19-9 (per unit)	2.71 (1.69–4.34)	< 0.001	2.30 (1.41–3.77)	< 0.001
MRI findings				
Tumor morphology (per category)	1.92 (1.18–3.13)	0.009		
Hepatic capsular retraction	0.32 (0.11–0.94)	0.039		
Biliary dilatation sign (per grade)	2.09 (1.46–2.99)	< 0.001	1.78 (1.22–2.60)	0.003

Values are odds ratios with 95% confidence intervals. Only variables with $P < 0.05$ in the univariable analysis were entered into the multivariable backward stepwise logistic regression. PNI, perineural invasion.

3.4 Predictive performance, calibration and clinical utility

The AUCs of the clinical-imaging, radiomics and multimodal models were 0.721 (95% CI 0.628–0.810), 0.883 (0.828–0.930) and 0.906 (0.859–0.947) in the training cohort, 0.597 (95% CI 0.438–0.750), 0.815 (0.704–0.898) and 0.823 (0.706–0.910) in the testing cohort, and 0.779 (95% CI 0.678–0.872), 0.843 (0.761–0.913) and 0.869 (0.800–0.928) in the validation cohort (Table 3 and Fig. 5). With the threshold fixed at the training-cohort Youden index, the multimodal model had the highest sensitivity in the training and validation cohorts (85.7% and 90.0%), whereas the radiomics model had the highest specificity (89.5%, 86.1% and 85.1%) and positive predictive value (60.8%, 50.0% and 60.0%); negative predictive values were high for all three models (84.5%–96.3%), indicating that their main value lies in excluding PNI. DeLong tests showed that the radiomics and multimodal models outperformed the clinical-imaging model in the training and testing cohorts ($P = 0.003$ and $P < 0.001$; $P = 0.032$ and $P = 0.006$); full pairwise results are given in Supplementary Tables S3. The clinical-imaging model performed least well in the testing cohort, whereas the radiomics and multimodal models remained comparatively stable across cohorts.

Table 3
Diagnostic performance of the clinical-imaging, radiomics and multimodal models in the three cohorts.

Model	AUC (95% CI)	SEN, %	SPE, %	ACC, %	PPV, %	NPV, %
Training cohort (*n* = 232, PNI-positive = 42)						
Clinical-imaging model	0.721 (0.628–0.810)	59.5	78.4	75.0	37.9	89.8
Radiomics model	0.883 (0.828–0.930)	73.8	89.5	86.6	60.8	93.9
Multimodal model	0.906 (0.859–0.947)	85.7	82.1	82.8	51.4	96.3
Testing cohort (*n* = 99, PNI-positive = 20)						
Clinical-imaging model	0.597 (0.438–0.750)	55.0	62.0	60.6	26.8	84.5
Radiomics model	0.815 (0.704–0.898)	55.0	86.1	79.8	50.0	88.3
Multimodal model	0.823 (0.706–0.910)	75.0	70.9	71.7	39.5	91.8
Validation cohort (*n* = 124, PNI-positive = 30)						
Clinical-imaging model	0.779 (0.678–0.872)	76.7	71.3	72.6	46.0	90.5
Radiomics model	0.843 (0.761–0.913)	70.0	85.1	81.5	60.0	89.9
Multimodal model	0.869 (0.800–0.928)	90.0	74.5	78.2	52.9	95.9

ACC, accuracy; AUC, area under the receiver operating characteristic curve; NPV, negative predictive value; PPV, positive predictive value; SEN, sensitivity; SPE, specificity. The classification threshold was the point of the maximum Youden index in the training cohort and was applied unchanged to the testing and validation cohorts.

Calibration curves and the Hosmer-Lemeshow test indicated that predicted probabilities were generally close to observed PNI rates (Fig. 6A–C), and the Brier scores in the testing and validation cohorts (0.154/0.126/0.121 and 0.156/0.131/0.126) indicated better overall accuracy for the radiomics and multimodal models than for the clinical-imaging model. In decision curve analysis, the net benefit of all three models exceeded the treat-all and treat-none lines across the threshold range of 0.10–0.60, with a slight advantage for the multimodal model at lower thresholds (Fig. 6D–F). The multimodal model was visualized as a nomogram for individualized PNI risk prediction (Fig. 6G). The nomogram allows the probability of PNI to be estimated for an individual patient from the clinical-imaging and radiomics scores.

3.5 Survival analysis

The median follow-up was 4.2 years for OS and 4.8 years for RFS; 107 patients (23.5%) died and 113 patients (24.8%) developed recurrence. OS and RFS were both worse in PNI-positive than in PNI-negative patients (OS: log-rank *P* = 0.030, HR = 1.60, 95% CI 1.04–2.44; RFS: log-rank *P* = 0.034, HR = 1.57, 95% CI 1.03–2.38) (Fig. 7A, 7B).

With the median predicted probability of the multimodal model (0.086) as the cut-off, 227 patients were classified as low risk and 228 as high risk. Both OS and RFS were significantly worse in the high-risk group (OS: log-rank *P* = 0.004, HR = 1.77, 95% CI 1.20–2.63; RFS: log-rank *P* = 0.007, HR = 1.67, 95% CI 1.14–2.43) (Fig. 7C, 7D). The one-, three- and five-year OS and RFS rates of each subgroup are summarized in Table 4. The 5-year OS rate was 76.4% in PNI-negative versus 69.7% in PNI-positive patients (80.6% versus 69.4% for the low- and high-risk groups), and the corresponding 5-year RFS rates were 73.4% versus 61.4% and 76.9% versus 64.9%.

Table 4
One-, three- and five-year overall and recurrence-free survival of the 455 patients.

OS	**PNI negative (*n* = 363)**	**PNI positive (*n* = 92)**	**Low-risk group (*n* = 227)**	**High-risk group (*n* = 228)**
Events, *n*	78	29	41	66
1-year OS rate, % (95% CI)	91.4 (88.0–93.9)	82.6 (73.2–89.0)	92.9 (88.7–95.6)	86.4 (81.2–90.2)
3-year OS rate, % (95% CI)	80.1 (75.3–84.0)	71.8 (61.1–80.0)	83.4 (77.4–87.9)	73.5 (67.1–78.9)
5-year OS rate, % (95% CI)	76.4 (71.0–80.9)	69.7 (58.4–78.5)	80.6 (73.9–85.8)	69.4 (62.3–75.5)
HR (95% CI)	Reference	1.60 (1.04–2.44)	Reference	1.77 (1.20–2.63)
log-rank *P*		0.030		0.004
Median follow-up, years	4.4	3.4	4.3	4.1
RFS	PNI negative (*n* = 363)	PNI positive (*n* = 92)	Low-risk group (*n* = 227)	High-risk group (*n* = 228)
Events, *n*	83	30	45	68
1-year RFS rate, % (95% CI)	83.3 (78.8–86.9)	73.1 (62.0–81.4)	87.5 (82.1–91.3)	75.0 (68.4–80.4)
3-year RFS rate, % (95% CI)	75.2 (69.9–79.6)	61.4 (49.5–71.4)	78.3 (71.8–83.6)	66.4 (59.2–72.6)
5-year RFS rate, % (95% CI)	73.4 (68.0–78.0)	61.4 (49.5–71.4)	76.9 (70.2–82.4)	64.9 (57.5–71.3)
HR (95% CI)	Reference	1.57 (1.03–2.38)	Reference	1.67 (1.14–2.43)
log-rank *P*		0.034		0.007
Median follow-up, years	4.8	4.2	4.7	5.0

Values are Kaplan-Meier estimates with 95% confidence intervals. HR, hazard ratio; OS, overall survival; PNI, perineural invasion; RFS, recurrence-free survival. Risk groups were defined by the median predicted probability of the multimodal model.

4. Discussion

In this study of 455 patients with ICC, features were selected separately for each phase of multiphasic contrast-enhanced MRI and combined for modeling. The radiomics model predicted PNI more effectively

than the clinical-imaging model based on conventional clinical and imaging findings, and the multimodal model integrating both achieved the highest AUC. Radiomics-based risk stratification and PNI status both discriminated postoperative OS and RFS, and the radiomics model provided greater net benefit than the clinical-imaging model over a wide range of threshold probabilities. Because all inputs come from routine clinical data and preoperative MRI, the model can be integrated into existing diagnostic workflows.

Compared with previous studies, the multimodal model showed better performance in independent datasets. Previous studies on PNI prediction in ICC were mostly based on contrast-enhanced CT or a single MRI sequence, and their performance declined markedly in independent validation: the MRI-based fusion model reported by Qi et al. achieved an AUC of 0.905 in the training set but only 0.760 externally [23], and the multicenter radiomics model of Liu et al. achieved AUCs of 0.748 and 0.729 in external validation and a prospective cohort [12]. In the present study, the radiomics and multimodal models achieved AUCs of 0.815 and 0.843 in the testing cohort and 0.823 and 0.869 in the validation cohort, which are higher than those reported above and consistent across two independent cohorts. This difference may reflect the use of a single imaging modality or phase and differences in the validation strategy. Selecting features separately in the four phases (T2WI, AP, PVP and DP) before modeling reduces collinearity between phases and clarifies the contribution of each phase across tumor parenchyma, blood supply and enhancement, which is difficult to achieve with a single phase or contrast-enhanced CT. The prognostic value of the model for OS and RFS further extends multimodal radiomics from preoperative prediction to postoperative management.

In the clinical-imaging model, Log10 CA19-9 and the biliary dilatation sign were independent predictors. CA19-9 is the most widely used serum marker in ICC and has been associated with tumor burden, aggressiveness and postoperative survival, leading to its inclusion in prognostic nomograms and risk scores [24–26]. The biliary dilatation sign was the imaging finding most strongly associated with PNI (multivariable OR = 1.78; P = 0.003). Intrahepatic nerve bundles run with the bile ducts and portal vein within the Glisson capsule, and PNI is defined as tumor invasion along these nerve bundles [27]; large-duct-type ICC, which is closely related to mucin secretion, periductal infiltration and perineural invasion [28], corresponds to the mucin-producing bile duct tumor that secretes abundant viscous mucin and causes biliary dilatation [29]. Because this sign is assessed routinely on preoperative MRI, it can be reported without additional examination, and these observations are consistent with the anatomical proximity of the peribiliary nerve plexus to the dilated bile ducts. Among intraductal tumors, the tubular growth pattern shows more perineural and vascular invasion than the papillary pattern [30], and the population prevalence of PNI is inversely correlated with the proportion of mass-forming ICC, suggesting that non-mass-forming tumors are more prone to PNI [31]. The biliary dilatation sign therefore marks the large-duct peribiliary space that is rich in accompanying nerve bundles, which explains its independent association with PNI and supports its use in preoperative assessment. Conventional signs such as tumor morphology, hepatic capsular retraction, vessel penetration and adjacent organ invasion were partly significant in the univariable analysis but were not retained in the multivariable model, suggesting information overlap with CA19-9 and the biliary dilatation sign. Maximum tumor diameter and hepatitis B

virus infection were not independently associated with PNI, which differs from some reports that tumor size [32] and hepatitis B infection [33] affect ICC prognosis and may reflect the case composition and single-center sample of this cohort.

The radiomics model performed significantly better than the clinical-imaging model and remained stable in the testing and validation cohorts, suggesting that gray-level distribution and texture heterogeneity on multiphasic MRI reflect the biology of PNI. The 21 features were dominated by first-order statistics (15/21), with GLSZM, GLCM and shape features, indicating that PNI-positive tumors differ mainly in signal intensity distribution and regional homogeneity, consistent with their frequent fibrosis, biliary dilatation and mixed intratumoral components [4, 18, 34]. The preponderance of first-order features also suggests that signal intensity features are more informative than texture descriptors in this setting, and that multimodal integration captures complementary information. The multimodal model had the highest AUC in all three cohorts (0.906, 0.823 and 0.869), indicating that combining radiomic features with clinical-imaging information captures both tumor biology and the overall condition of the patient; this multimodal strategy is the main innovation relative to previous unimodal radiomics studies [12, 18].

Patients who were PNI-positive or were classified as high risk by the radiomics model had significantly worse OS and RFS, consistent with previous findings [6–10]; Zhang et al. reported that PNI was associated with OS and RFS after curative resection and suggested that PNI-positive patients might benefit from adjuvant chemotherapy [7], and the multicenter study of Wei et al. confirmed PNI as an independent adverse factor [6]. Stratification by the median probability of the multimodal model alone distinguished postoperative survival risk (OS: HR = 1.77; P = 0.004; RFS: HR = 1.67; P = 0.007), suggesting that preoperative radiomics assessment may also inform follow-up intensity and adjuvant treatment decisions. The median follow-up was 4.2–4.8 years, and the event rate was low (23.5% deaths and 24.8% recurrences); because the one-, three- and five-year rates were estimated from patients followed for the corresponding period, the survival results should be regarded as preliminary. The survival rates may also be overestimated: patients without follow-up records, including those who died early after surgery or were transferred to other hospitals and whose recurrence and survival data were not collected, were excluded from the cohort, which biased its composition towards a better prognosis; the reported OS and RFS rates therefore represent estimates for patients with complete follow-up and may be higher than the true rates among all patients undergoing curative resection. These findings suggest that the model may help to identify patients who could benefit from closer surveillance or adjuvant therapy. The direction and magnitude of the hazard ratios were similar for OS and RFS.

This study has several limitations. First, it was a single-center retrospective study; although a separate validation cohort was used, it came from the same institution, so selection bias and center effects may persist and multicenter prospective external validation across scanners and protocols is still required. Second, the PNI-positive rate was 20.2% and the testing cohort included only 99 patients (20 PNI-positive), so confidence intervals of the AUCs were wide and some comparisons may have lacked power. Third, the diagnosis of PNI relied on pathology reports and S-100 immunohistochemistry was not performed in all sections, which may have underestimated microscopic PNI. Fourth, manual delineation,

although assessed for agreement, is labor-intensive and restricts clinical implementation; automatic segmentation and end-to-end deep learning should be explored [14, 16, 17]. Fifth, peritumoral features and other modalities such as genomics were not included, although peritumoral features may further improve PNI prediction [18, 19]. The absence of an external multi-institutional cohort remains the principal limitation, and the reported performance may therefore be optimistic.

5. Conclusion

The radiomics model based on multiphasic contrast-enhanced MRI (T2WI, AP, PVP and DP) predicts PNI in ICC effectively before surgery, outperforms the clinical-imaging model based on conventional clinical and imaging findings, and shows good calibration and clinical net benefit, while the multimodal model achieves the highest AUC. Radiomics-based risk stratification and PNI status both discriminated postoperative OS and RFS, indicating the potential for preoperative risk stratification and individualized follow-up. Multicenter prospective validation and the incorporation of peritumoral features, deep learning and explainable artificial intelligence are required for clinical translation.

Declarations

Ethics approval and consent to participate:

This study was performed in accordance with the ethical standards of the Declaration of Helsinki. The protocol was approved by the Ethics Committee of the Eastern Hepatobiliary Surgery Hospital, the Third Affiliated Hospital of the Naval Medical University, China. For this retrospective study, the requirement for informed consent was waived by the Institutional Review Board (IRB).

Consent for publication:

Not applicable.

Competing interests:

The authors declare no competing interests

Funding:

This research did not receive any specific grant from funding agencies in the public, commercial, or not-for-profit sectors.

Author Contribution

NY, HD, LD conceived the project and designed the study. LHL, SH, SCZ performed the data extraction and collection. HD performed the data analysis and wrote the manuscript. SF, ZSS revised the

manuscript. All authors contributed to the article and approved the submitted version.

Acknowledgements:

Not applicable.

Data Availability

The datasets generated and/or analysed during the current study are not publicly available because they contain patient-level clinical and imaging data that are subject to institutional and ethical restrictions, but they are available from the corresponding author on reasonable request.

References

1. Florio AA, Ferlay J, Znaor A, et al. Global trends in intrahepatic and extrahepatic cholangiocarcinoma incidence from 1993 to 2012. Cancer. 2020;126(11):2666–78.
2. Saha SK, Zhu AX, Fuchs CS, Brooks GA. Forty-year trends in cholangiocarcinoma incidence in the U.S.: intrahepatic disease on the rise. Oncologist. 2016;21(5):594–9.
3. Gupta A, Dixon E. Epidemiology and risk factors: intrahepatic cholangiocarcinoma. Hepatobiliary Surg Nutr. 2017;6(2):101–4.
4. Chen SH, Zhang BY, Zhou B, et al. Perineural invasion of cancer: a complex crosstalk between cells and molecules in the perineural niche. Am J Cancer Res. 2019;9(1):1–21.
5. Sayyed Y, Ji R, Zaheer T, Li L. Pathology and molecular mechanisms of perineural spread of tumors. Med Res Arch. 2021;9(6):2457.
6. Wei T, Zhang XF, He J, et al. Prognostic impact of perineural invasion in intrahepatic cholangiocarcinoma: multicenter study. Br J Surg. 2022;109(7):610–6.
7. Zhang Z, Zhou Y, Hu K, et al. Perineural invasion as a prognostic factor for intrahepatic cholangiocarcinoma after curative resection and a potential indication for postoperative chemotherapy: a retrospective cohort study. BMC Cancer. 2020;20(1):270.
8. Meng XL, Lu JC, Zeng HY, et al. The clinical implications and molecular features of intrahepatic cholangiocarcinoma with perineural invasion. Hepatol Int. 2023;17(1):235–48.
9. Bartsch F, Heuft LK, Baumgart J, et al. Influence of lymphangio (L), vascular (V), and perineural (Pn) invasion on recurrence and survival of resected intrahepatic cholangiocarcinoma. J Clin Med. 2021;10(11):2426.
10. Zou M, Sheng J, Ruan M, et al. Perineural invasion confers poorer clinical outcomes in patients with T1/T2 intrahepatic cholangiocarcinoma: a single center, retrospective cohort study. J Hepatocell Carcinoma. 2023;10:2403–14.

11. Brunese MC, Fantozzi MR, Fusco R, et al. Update on the applications of radiomics in diagnosis, staging, and recurrence of intrahepatic cholangiocarcinoma. Diagnostics. 2023;13(8):1488.
12. Liu Z, Luo C, Chen X, et al. Noninvasive prediction of perineural invasion in intrahepatic cholangiocarcinoma by clinicoradiological features and computed tomography radiomics based on interpretable machine learning: a multicenter cohort study. Int J Surg. 2024;110(2):1178–89.
13. Zhan PC, Lyu PJ, Li Z, et al. CT-based radiomics analysis for noninvasive prediction of perineural invasion of perihilar cholangiocarcinoma. Front Oncol. 2022;12:900478.
14. Xu L, Chen Z, Zhu D, Wang Y. The application status of radiomics-based machine learning in intrahepatic cholangiocarcinoma: systematic review and meta-analysis. J Med Internet Res. 2025;27:e69906.
15. Chen PY, Yang Z, Zhang H, et al. Personalized intrahepatic cholangiocarcinoma prognosis prediction using radiomics: application and development trend. Front Oncol. 2023;13:1133867.
16. Avanzo M, Wei L, Stancanello J, et al. Machine and deep learning methods for radiomics. Med Phys. 2020;47(5):e185–202.
17. Cheng M, Zhang H, Guo Y, et al. Comparison of MRI and CT based deep learning radiomics analyzes and their combination for diagnosing intrahepatic cholangiocarcinoma. Sci Rep. 2025;15(1):8246.
18. Sun Y, Li Y, Li M, et al. Radiomics analysis using machine learning to predict perineural invasion in pancreatic cancer. BMC Cancer. 2025;25(1):852.
19. Xie N, Fan XH, Chen D, et al. Peritumoral and intratumoral texture features based on multiparametric MRI and multiple machine learning methods to preoperatively evaluate the pathological outcomes of pancreatic cancer. J Magn Reson Imaging. 2022;57(5):1440–53.
20. Tibshirani R. Regression shrinkage and selection via the lasso. J R Stat Soc B. 1996;58(1):267–88.
21. DeLong ER, DeLong DM, Clarke-Pearson DL. Comparing the areas under two or more correlated receiver operating characteristic curves: a nonparametric approach. Biometrics. 1988;44(3):837–45.
22. Vickers AJ, Elkin EB. Decision curve analysis: a novel method for evaluating prediction models. Med Decis Mak. 2006;26(6):565–74.
23. Qi Z, Yuan H, Li Q, et al. An MRI-based fusion model for preoperative prediction of perineural invasion status in patients with intrahepatic cholangiocarcinoma. World J Surg Oncol. 2025;23(1):164.
24. Wang Y, Li J, Xia Y, et al. Prognostic nomogram for intrahepatic cholangiocarcinoma after partial hepatectomy. J Clin Oncol. 2013;31(9):1188–95.
25. Asaoka T, Kobayashi S, Hanaki T, et al. Clinical significance of preoperative CA19-9 and lymph node metastasis in intrahepatic cholangiocarcinoma. Surg Today. 2020;50(10):1176–86.
26. Wang XY, Zhu WW, Lu L, et al. Development and validation of a mutation-annotated prognostic score (MAPS) for intrahepatic cholangiocarcinoma after resection: a retrospective cohort study. Int J Surg. 2023;109(11):3506–18.

27. Kami S, Kojima M, Kudo M, et al. Clinicopathological significance and prognostic impact of perineural invasion in intrahepatic cholangiocarcinoma: a single-center, retrospective study. Hum Pathol. 2025;166:105952.
28. Sigel CS, Drill E, Zhou Y, et al. Intrahepatic cholangiocarcinomas have histologically and immunophenotypically distinct small and large duct patterns. Am J Surg Pathol. 2018;42(10):1334–45.
29. Lim JH, Jang KT. Mucin-producing bile duct tumors: radiological-pathological correlation and diagnostic strategy. J Hepatobiliary Pancreat Sci. 2010;17(3):223–9.
30. Tsukahara T, Shimoyama Y, Ebata T, et al. Cholangiocarcinoma with intraductal tubular growth pattern versus intraductal papillary growth pattern. Mod Pathol. 2016;29(3):293–301.
31. Kolck J, Auer TA, Pedersen CW, et al. Perineural invasion in intrahepatic cholangiocarcinoma: meta-analysis of prevalence, association with tumor features, and impact on survival. JHEP Rep. 2026;8(9):101939.
32. Kong J, Cao Y, Chai J, et al. Effect of tumor size on long-term survival after resection for solitary intrahepatic cholangiocarcinoma. Front Oncol. 2021;10:559911.
33. Zhou HB, Wang H, Li YQ, et al. Hepatitis B virus infection: a favorable prognostic factor for intrahepatic cholangiocarcinoma after resection. World J Gastroenterol. 2011;17(10):1292–303.
34. Fu Y, Shen K, Wang H, et al. Alpha5 nicotine acetylcholine receptor subunit promotes intrahepatic cholangiocarcinoma metastasis. Signal Transduct Target Ther. 2024;9(1):55.

Figures

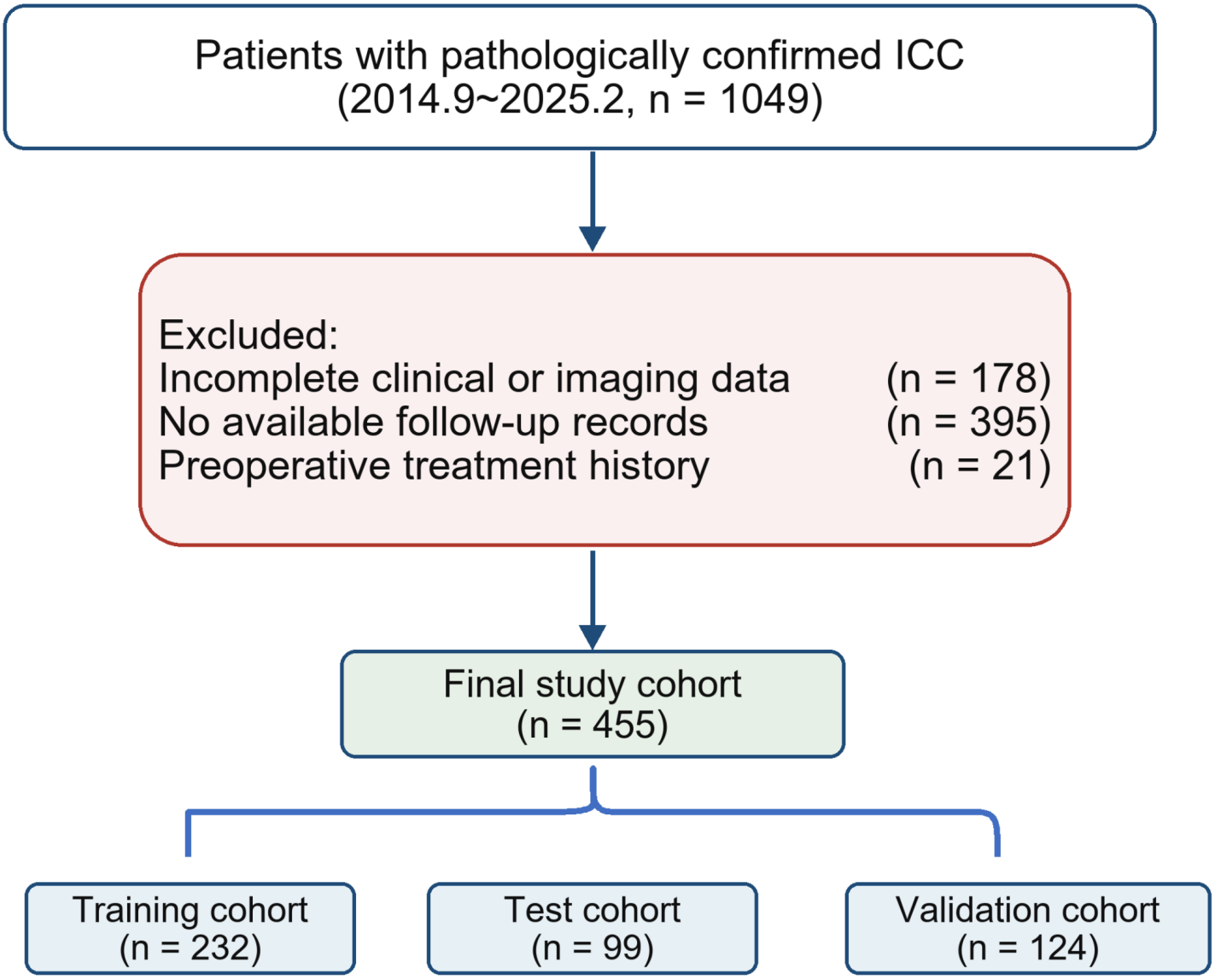


Figure 1

Flow chart of patient selection and grouping

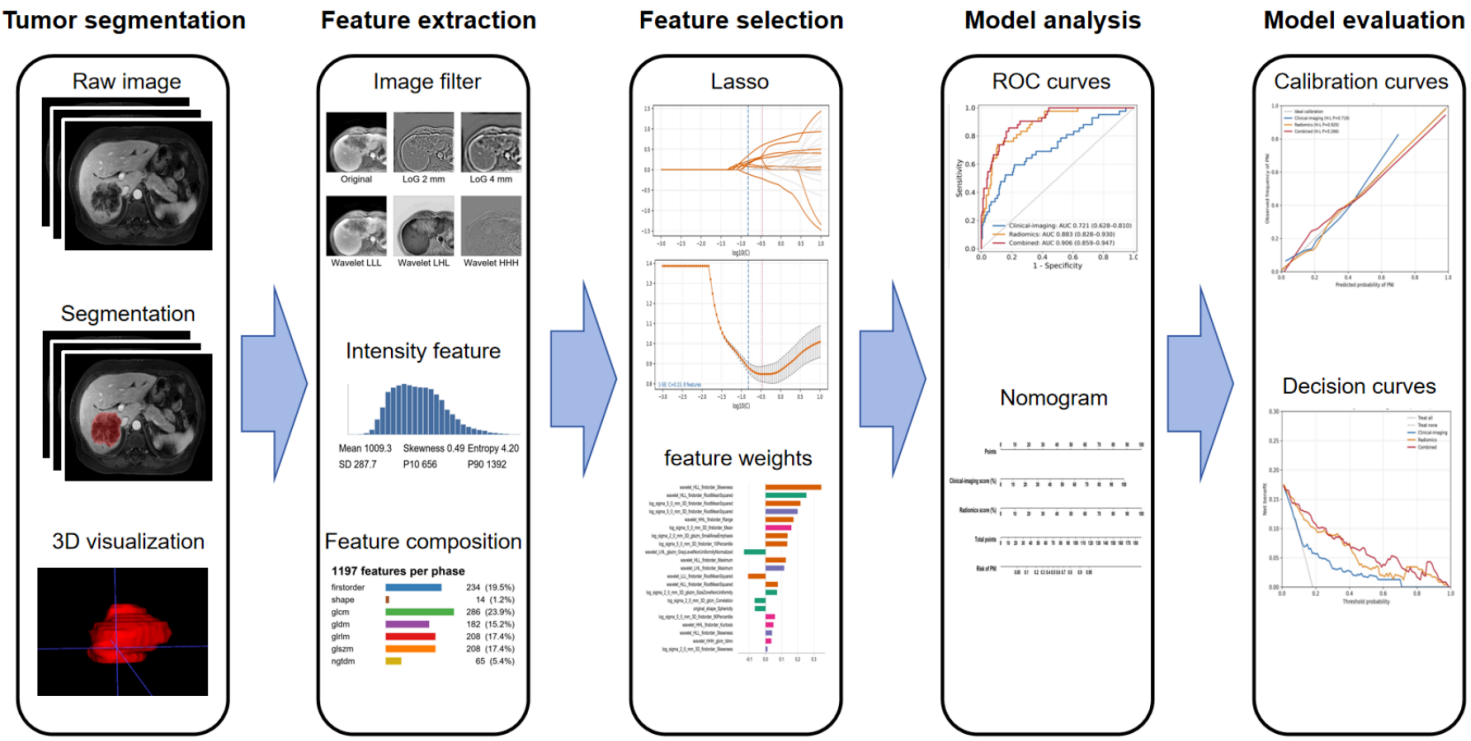


Figure 2

Workflow of the radiomics analysis

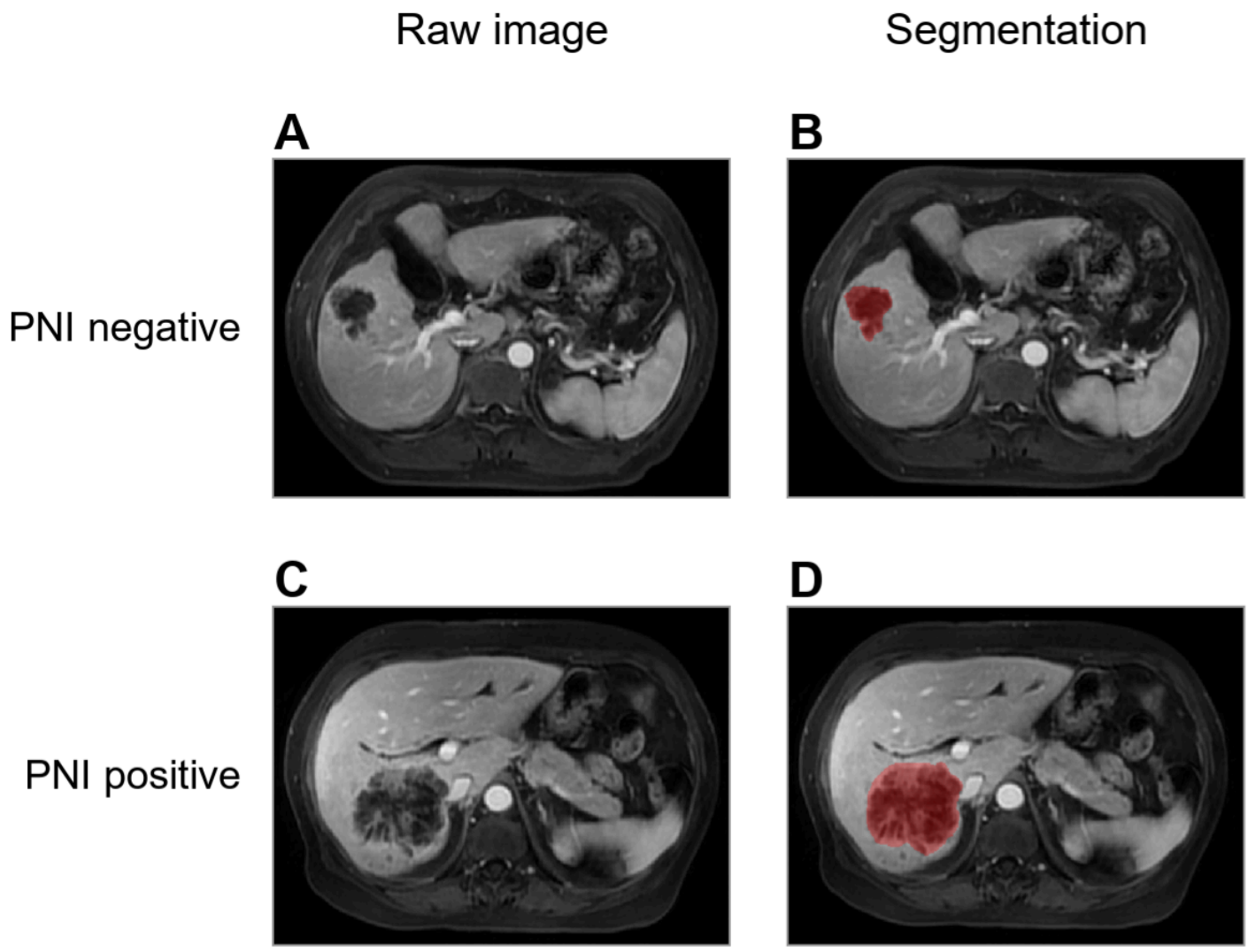


Figure 3

Representative MRI images and tumor regions of interest (portal venous phase, PVP). (A, B) A PNI-negative case and (C, D) a PNI-positive case; the left column (A, C) shows the original images and the right column (B, D) the tumor regions of interest (semi-transparent red overlay). The remaining phases are shown in Figure S1. PNI, perineural invasion.

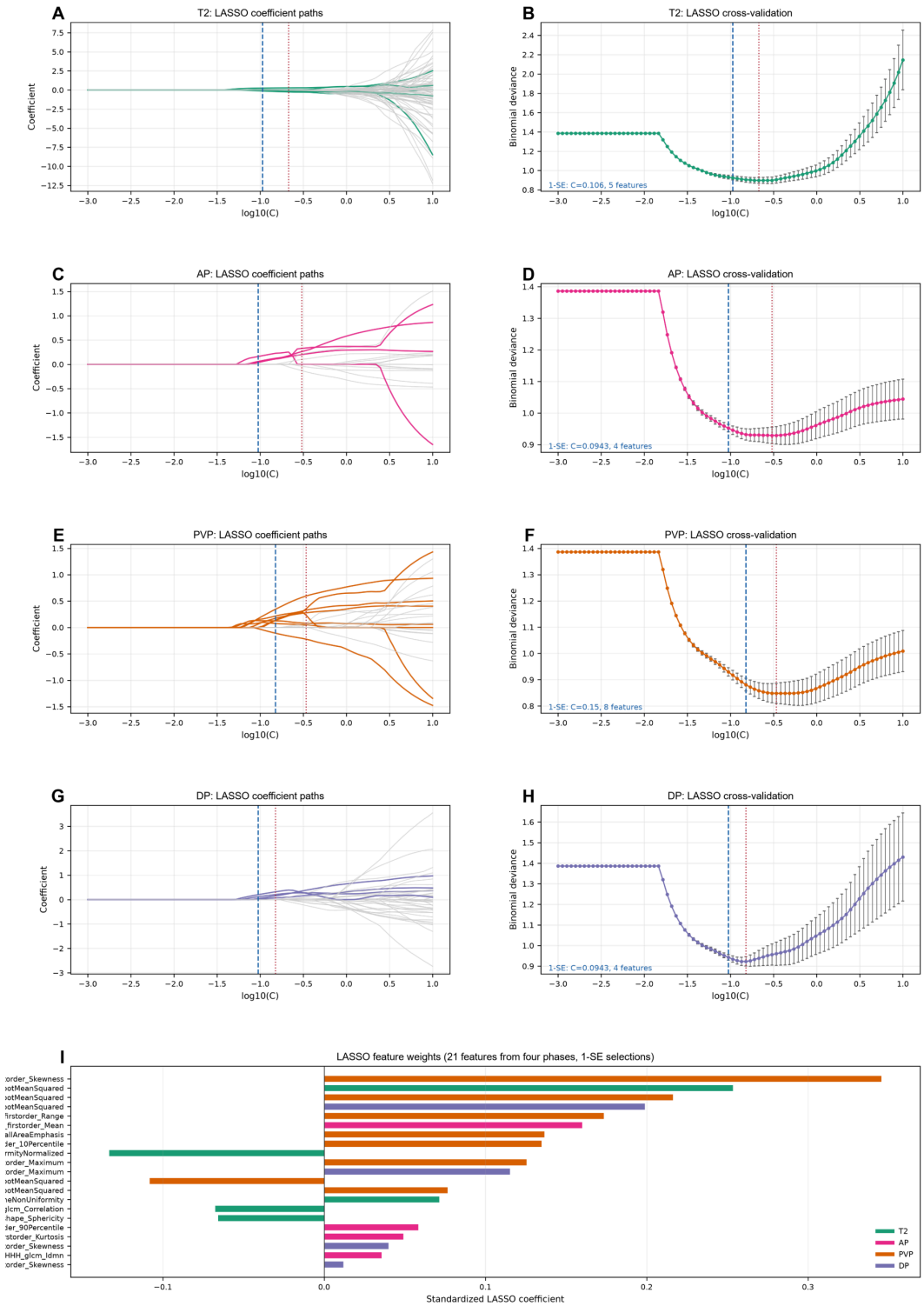


Figure 4

Per-phase feature selection. (A, C, E, G) LASSO coefficient paths and (B, D, F, H) cross-validation curves for the T2-weighted, arterial, portal venous and delayed phases (the vertical lines mark the 1-SE point); (I) weights of the 21 selected radiomics features. LASSO, least absolute shrinkage and selection operator; 1-SE, one standard error; T2WI, T2-weighted imaging; AP, arterial phase; PVP, portal venous phase; DP, delayed phase.

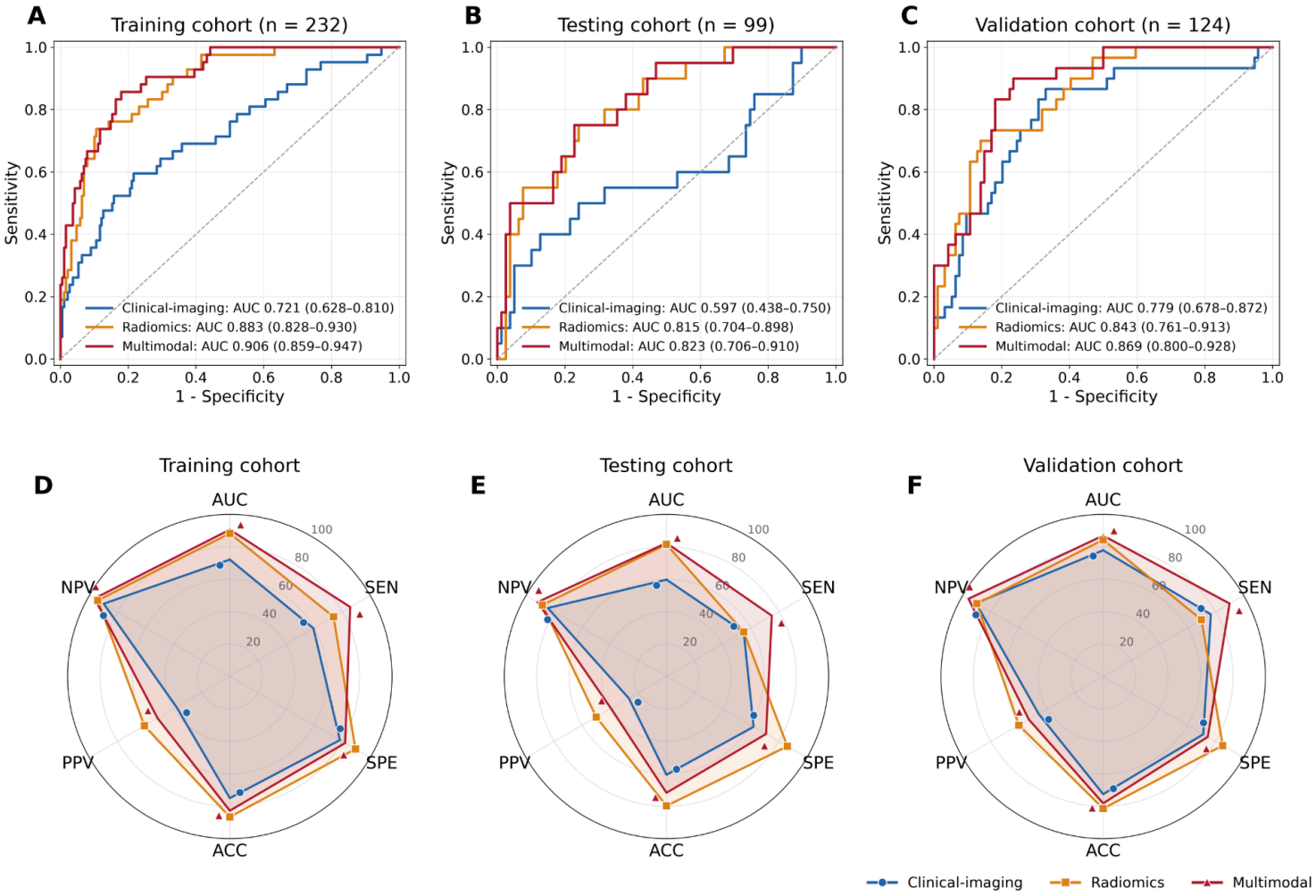


Figure 5

Diagnostic performance of the three models. (A-C) ROC curves and (D-F) radar plots of AUC, sensitivity, specificity, accuracy, PPV and NPV for the training, testing and validation cohorts. ACC, accuracy; AUC, area under the receiver operating characteristic curve; NPV, negative predictive value; PPV, positive predictive value; SEN, sensitivity; SPE, specificity.

Figure 6. Calibration curves (LOESS) and decision curve analysis

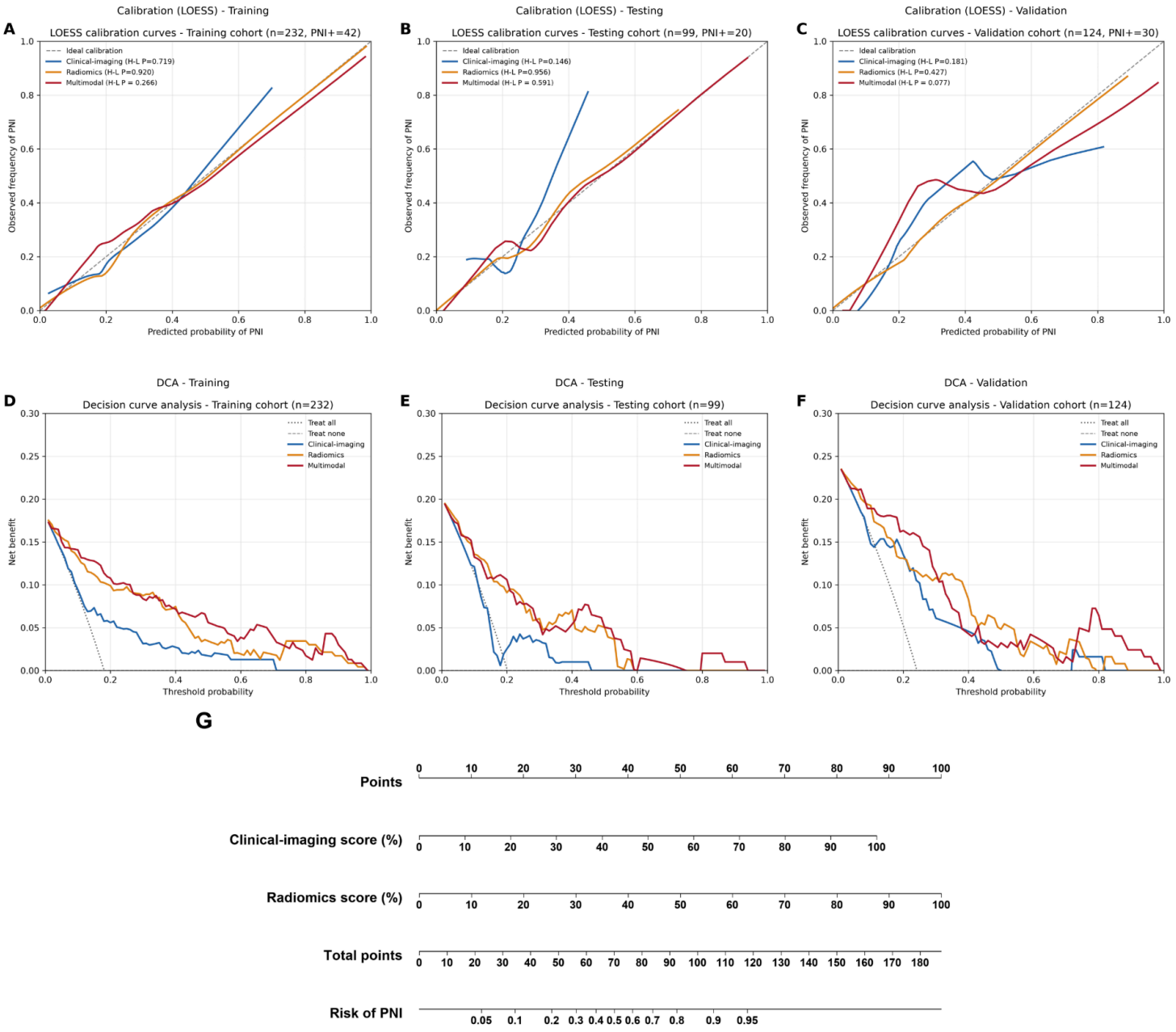


Figure 6

Calibration, clinical utility and nomogram. (A-C) LOESS calibration curves and (D-F) decision curve analysis in the training, testing and validation cohorts, with the treat-none and treat-all reference lines; (G) nomogram based on the clinical-imaging and radiomics scores. DCA, decision curve analysis; LOESS, locally weighted regression; PNI, perineural invasion.

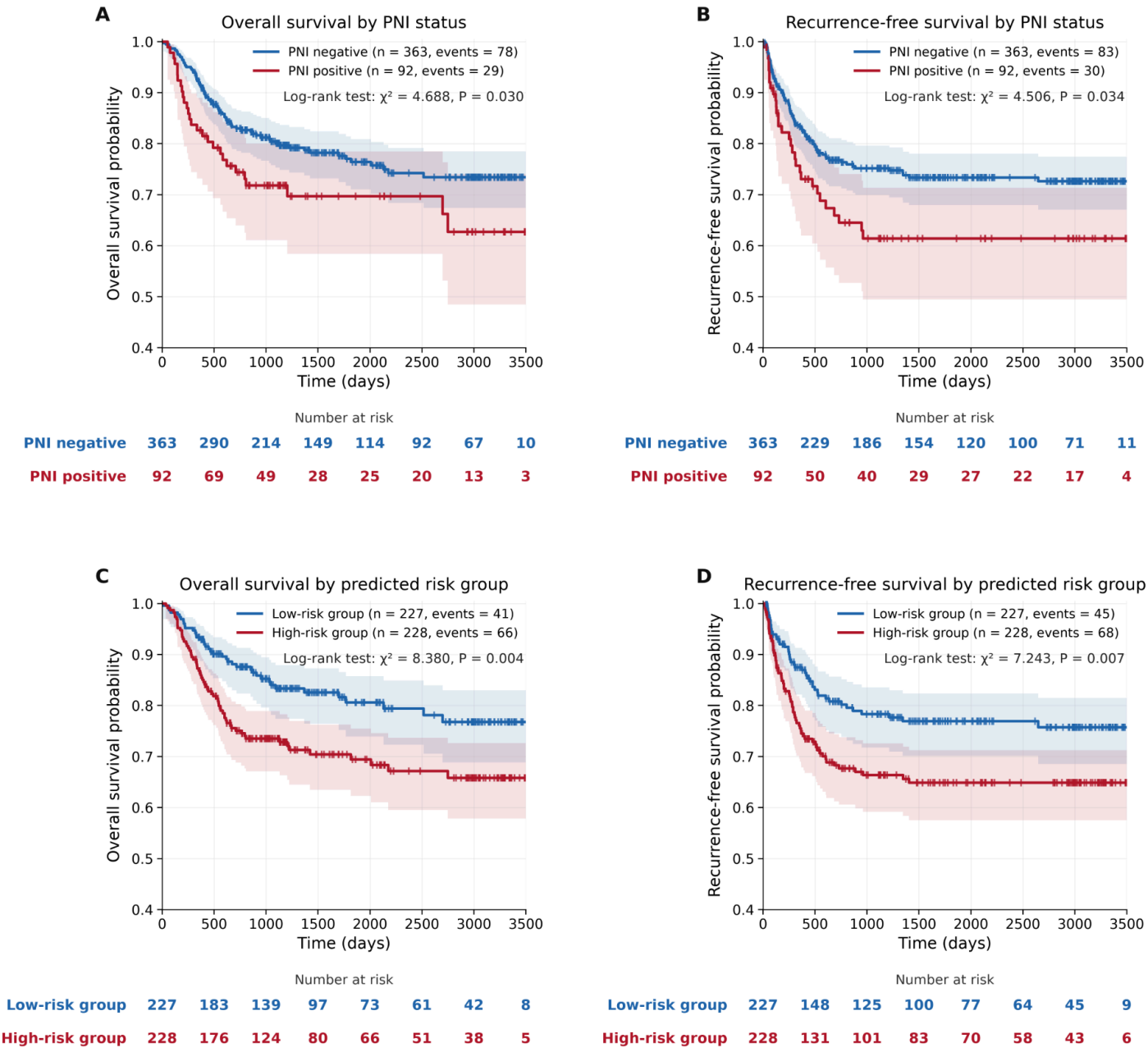


Figure 7

Kaplan-Meier curves of the 455 patients. (A) Overall survival and (B) recurrence-free survival by PNI status; (C) overall survival and (D) recurrence-free survival by multimodal-model risk group (median cut-off). Curves and numbers at risk are displayed up to 3500 days. HR, hazard ratio; OS, overall survival; PNI, perineural invasion; RFS, recurrence-free survival; the risk groups were defined by the median predicted probability of the multimodal model.

Supplementary Files

This is a list of supplementary files associated with this preprint. Click to download.

- TableS1.docx
- TableS2.docx
- FigureS1.png
- TableS3.docx
- FigureS1.png